# Parameterization of land surface albedo

**Shengcheng Cui (崔生成)[1], Zhen Wang (王 震)[2], and Shizhi Yang (杨世植)[1]**

*[1]Key Laboratory of Optical Calibration and Characterization, Anhui Institute of Optics and Fine Mechanics, Chinese Academy of Sciences, Hefei 230031, China*
*[2]College of Atmospheric Physics, Nanjing University of Information Science and Technology, Nanjing 210044, China*
*Corresponding author: shchcui@126.com*

Received March 6, 2014; accepted August 22, 2014; posted online October 27, 2014

Remote measurements of Earth's surface from ground, airborne, and spaceborne instruments show that its albedo is highly variable and is sensitive to solar zenith angle (SZA) and atmospheric opacity. Using a validated radiative transfer calculating toolbox, DISORT and a bidirectional reflectance distribution function library, AMBRALS, a land surface albedo (LSA) lookup table (LUT) is produced with respect to SZA and aerosol optical depth. With the LUT, spectral and broadband LSA can be obtained at any given illumination geometries and atmospheric conditions. It provides a fast and accurate way to simulate surface reflectance over large temporal and spatial scales for climate study.

*OCIS codes: 010.1310, 280.1310, 240.5698, 350.5610.*
*doi: 10.3788/COL201412.110101.*

Land surface albedo (LSA), characterizing the energy balance in the coupled surface–atmosphere system (CSAS), is required by climate models at various spatial scales from meters to kilometers[1,2]. Owing to its strong feedback effects, LSA is also important for determining atmospheric conditions in the boundary layer.

To facilitate application of satellite-derived surface albedos to climate studies, much research has been done on products validation[3], accuracy assessment[4–6], and method improvements[7]. Recently, efforts on the albedo parameterization over ocean surface have been made using the coupled ocean–atmosphere radiative transfer (RT) code[8,9]. However, the parameterization of LSA is still based on the assumption of isotropic diffuse skylight when calculating the surface blue-sky albedo[10]. Recently, the concept of anisotropic sky radiation has been proposed and preliminary results have been obtained[11,12].

With emphasis on the importance of considering anisotropic distribution of sky radiation, impacts of diffuse skylight on the LSA estimation have been studied[12]. Aiming to parameterize LSA for RT and climate modeling, we first simulated the angular distribution of sky radiation using a benchmark Monte Carlo RT (MCRT) model[13,14], which accounts for three-dimensional (3D) atmospheric effects. The simulated results gave us full proof of coupling diffuse skylight to LSA model. Then, a rigorous anisotropic LSA remote sensing model was constructed and LSA lookup table (LUT) was generated by coupling the DISORT code[15] and the bidirectional reflectance distribution function (BRDF) assembly library[6]. This object is to provide a fast and accurate LSA parameterization for soil–vegetation–atmosphere transfer and climate modeling.

To solve the 3D atmosphere effect on the RT processes, the state of the art in modeling this effect is the Monte Carlo technique, which is often used as the benchmark for testing and validating other RT models. Recently, a newly developed 3D MCRT model has been validated and evaluated via the intercomparisons between the MCARaTS[16], SHADOM[17], and SHARM-3D models[18]. It is found to be accurate in the RT simulations for the CSAS, including the characterization of the angular distribution of the irradiance field[13,14].

Figure 1 shows diffuse skylight distributions for four different aerosol/cloud atmospheres at 550 nm with an illumination angle at 60°, simulated using the 3D MCRT model[13,14]. From the simulations, one can easily find that the angular distribution of diffuse sky irradiance exhibits different degrees of anisotropic properties. This finding still holds true throughout the solar spectrum. From the RT theory, atmospheric particles, such as aerosols, clouds, and air molecules, that all have anisotropic scattering phase function, affect the radiation field in the atmosphere, resulting in the variation of intensity in different propagation directions.

On the other hand, the underlying surface also exhibits anisotropic light-scattering (reflecting) behaviors, strongly depending on the geometries between the illumination and the viewing direction. This anisotropic surface reflectivity may further modulate the outgoing electromagnetic waves by the trapping mechanism, corresponding to the successive reflections and scatterings between the atmosphere and the underlying surfaces, and have a considerable effect on the distribution of sky radiation[12,19]. In this context, the atmospheric radiation is in nature anisotropic.

Recent measurements from NASA airborne cloud absorption radiometer instruments demonstrate that BRDF of the CSAS is anisotropic[20]. The agreement between the airborne observations and our simulation

 

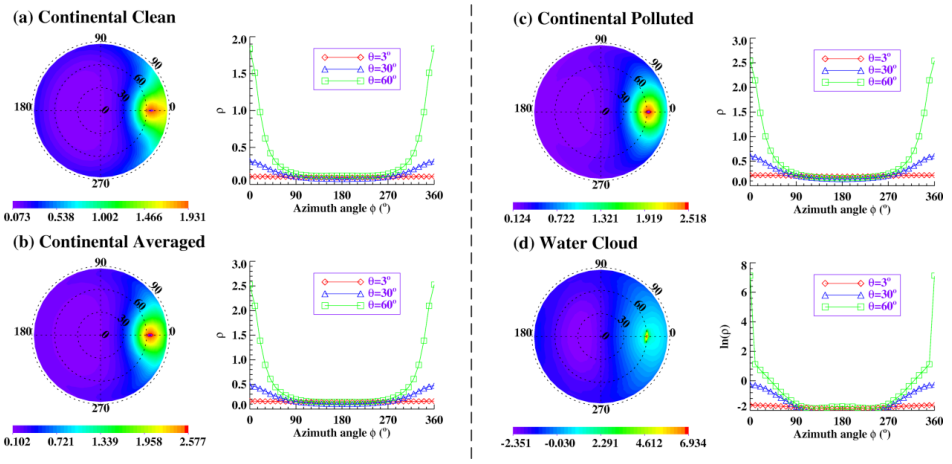


Fig. 1. Angular distribution of diffuse sky radiance for: (a) continental clean, (b) continental averaged, (c) continental polluted, and (d) water cloud atmospheres.

results indicates that it is rational and sound for us to take the anisotropic diffuse skylight into account when constructing optical remote sensing LSA model for the CSAS.

By taking into account the angular distribution of sky radiance, the LSA remote sensing model can be constructed as

$$\alpha_{\text{ani}}(\lambda)=\left(1-f_{\text{dt}}(\theta_{\text{s}};\tau,\lambda)\right)\alpha_{\text{DHR}}(\theta_0,\lambda)+f_{\text{dt}}(\theta_{\text{s}};\tau,\lambda)\alpha_{\text{BHR}_{\text{ani}}}(\lambda), \quad (1)$$

where the directional–hemispherical reflectance (DHR, also called black-sky albedo) and the bi-hemispherical reflectance (BHR, also called white-sky albedo) are respectively described as

$$\alpha_{\text{DHR}}(\theta_{\text{s}},\lambda)=\frac{1}{\pi}\int_0^{2\pi}\mathrm{d}\varphi_{\text{v}}\int_0^1\rho(\theta_{\text{s}},\varphi_{\text{s}},\theta_{\text{v}},\varphi_{\text{v}};\lambda)\mu_{\text{v}}\mathrm{d}\mu_{\text{v}}, \quad (2)$$

$$\alpha_{\text{BHR}_{\text{ani}}}(\lambda)=\frac{1}{\pi}\int_0^{2\pi}\int_0^1\Xi(\theta_{\text{s}},\varphi_{\text{s}};\tau,\lambda)\alpha_{\text{DHR}}(\theta_{\text{s}},\lambda)\mu_{\text{s}}\mathrm{d}\mu_{\text{s}}\mathrm{d}\varphi_{\text{s}}, \quad (3)$$

where $\theta_{\text{s}}$, $\varphi_{\text{s}}$ and $\theta_{\text{v}}$, $\varphi_{\text{v}}$ are the zenith and azimuth angles for illumination and viewing directions, respectively, $\mu$ is the cosine value of the zenith angle, $\lambda$ is the wavelength, $\tau$ is the aerosol optical depth (AOD) at 550 nm, $f_{\text{dt}}$ is the fraction of diffuse to total downward flux density, which is a function of AOD and solar zenith angle (SZA) $\theta_{\text{s}}$, and $\Xi$ is a function characterizing angular distribution of diffuse sky radiation. To model the radiance for different optical depths over different illumination and viewing angles, the DISORT code is used. $\rho(\theta_{\text{s}}, \varphi_{\text{s}}, \theta_{\text{v}}, \varphi_{\text{v}}; \lambda)$ denotes the spectral bidirectional reflectance factor, which can be modeled by a three-term superposed linear BRDF model[12]

$$\rho(\theta_{\text{s}},\theta_{\text{v}},\phi;\lambda)=f_{\text{iso}}(\lambda)+f_{\text{vol}}(\lambda)K_{\text{vol}}(\theta_{\text{s}},\theta_{\text{v}},\phi)+f_{\text{geo}}(\lambda)K_{\text{geo}}(\theta_{\text{s}},\theta_{\text{v}},\phi), \quad (4)$$

with $\phi=|\varphi_{\text{v}}-\varphi_{\text{s}}|$ representing the relative azimuth between the solar and the viewing azimuth, where $f_{\text{iso}}$, $f_{\text{geo}}$, and $f_{\text{vol}}$ are the weights given to the models geometric-optics (GO) kernel $K_{\text{geo}}$ and the RT volumetric (RTV) kernel $K_{\text{vol}}$.

Figure 2 depicts the proportion of diffuse irradiance under a black surface under different SZA and AOD. Both the SZA and the AOD have great effects on $f_{\text{dt}}$. The diffuse components predominates the whole downward irradiance field at low sun. This can be interpreted as the path that the photon traveled through the atmosphere is lengthened. This lengthening makes it more probable for the photon–aerosol collision. Moreover, the possibility of the aerosol–radiation interaction increases in more turbid atmospheres. For the sun above horizon with SZA nearly 75° and AOD approximating 0.5, $f_{\text{dt}}$ can reach as much as about 62.6%. This percentage can be much more as the SZA and AOD increase. Therefore, at large SZAs, the longer path length of light in the atmosphere increases multiple scattering and the proportion of diffuse radiance with increasing AOD.

With the physical definitions of the DHR and the BHR, and substituting Eq. (4) into Eqs. (2) and (3), respectively, we have

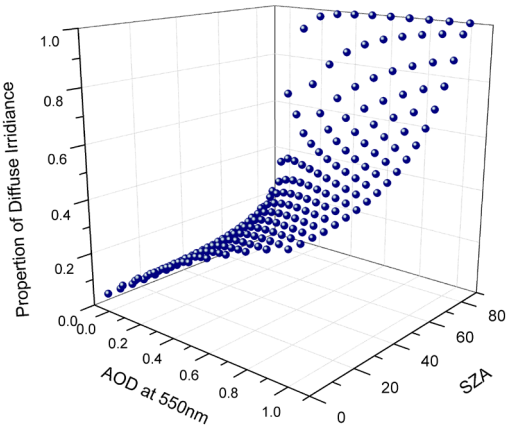


Fig. 2. Sensitivity of the diffuse irradiance to SZA and AOD (550 nm).

 

**Table 1.** Coefficients for Converting MODIS First Seven Spectral Albedo to SWA

| SWA | Conversion Coefficients | | | | | | | |
|---|---|---|---|---|---|---|---|---|
| | $c_1$ | $c_2$ | $c_3$ | $c_4$ | $c_5$ | $c_6$ | $c_7$ | $c_0$ |
| Snow-free Surface | 0.3973 | 0.2382 | 0.3489 | –0.2655 | 0.1604 | –0.0138 | 0.0682 | 0.0036 |
| Snow-covered Surface | 0.1574 | 0.2789 | 0.3829 | – | 0.1131 | – | 0.0694 | -0.0093 |

$$\alpha_{\mathrm{DHR}}(\theta_s,\lambda) = f_{\mathrm{iso}}(\lambda) + f_{\mathrm{vol}}(\lambda) h_{\mathrm{vol}}(\theta_s) + f_{\mathrm{geo}}(\lambda) h_{\mathrm{geo}}(\theta_s), \quad (5)$$

$$\alpha_{\mathrm{BHR_{ani}}}(\lambda) = f_{\mathrm{iso}}(\lambda) + f_{\mathrm{vol}}(\lambda) H_{\mathrm{vol}} + f_{\mathrm{geo}}(\lambda) H_{\mathrm{geo}}(\theta_s), \quad (6)$$

where the BRDF kernel angular integrals can be pre-calculated by

$$h_k(\theta_s) = \frac{1}{\pi}\int_0^{2\pi}\int_0^{\pi/2} K_k(\theta_s,\theta_v,\phi)\sin\theta_v\cos\theta_v \mathrm{d}\theta_v \mathrm{d}\phi, \quad (7)$$

$$H_k = \frac{2}{\pi}\int_0^{\pi/2}\int_0^{2\pi}\int_0^{\pi/2} \Xi(\theta_s,\varphi_s;\tau,\lambda) K_k(\theta_s,\theta_v,\phi)\sin\theta_v\cos\theta_v\sin\theta_s\cos\theta_s \mathrm{d}\theta_v \mathrm{d}\phi \mathrm{d}\theta_s. \quad (8)$$

By tabulating Eqs. (7) and (8) into LUT form, the computation speed improves by a factor of about 2000 as compared with the original analytical form. With the spectral angular integrals of the BRDF kernels, the shortwave albedo (SWA) is obtained via a spectral-to-broadband conversion scheme for snow-free and snow-covered surfaces, respectively[21]:

$$\alpha_{\mathrm{sw}} = \sum_{i=1}^{N} c_i \alpha_{\mathrm{ani},i} + c_0. \quad (9)$$

Table 1 lists the coefficients for calculating SWA (0.3–5.0 $\mu$m) from moderate-resolution imaging spectroradiometer (MODIS) spectral albedo (bands 1–7). Thus, a parameterization of LSA can be achieved with the anisotropic LSA remote sensing model and the angular integrals mentioned above.

Based on the model calculations, LSA is most sensitive to SZA and AOD. Here we tabulated LSA as a function of these two parameters only. The LUT has 209 records (11×19) representing 11 AODs and 19 SZAs. Users can easily get spectral and broadband albedo by an interpolation technique using any combination of the two variables with BRDF model parameters obtained.

As can be seen from Eq. (1), the developed LSA model is the function of both SZA and AOD. By fixing any one of these two variables, we can get the sensitivity of the model to another one. Therefore, when fixing the variable SZN, the sensitivity of the LSA model to the AOD at 550 nm can be obtained, and correspondingly, the relationship can be built as

$$\frac{\partial \alpha_{\mathrm{ani}}}{\partial \tau} = \frac{\partial f_{\mathrm{dt}}}{\partial \tau}\left(\alpha_{\mathrm{BHR_{ani}}} - \alpha_{\mathrm{DHR}}\right) + \frac{\partial \alpha_{\mathrm{BHR_{ani}}}}{\partial \tau} f_{\mathrm{dt}}. \quad (10)$$

For our model, a 10% bias in the AOD estimation at 550 nm wavelength will induce 0.22%, –0.3%, and –3.51% biases in SWA calculation when fixing SZN at 45°, 60°, and 75°, respectively. The sensitivity for the first case is consistent with our previous work carried out using 550 nm POLDER measurements[12]. Consequently, the improvement of the AOD retrieval will to a certain extent favor estimating the LSA at low sun with SZN larger than 50° more accurately, especially in high latitudinal zones.

As shown by the curves in Fig. 3 for the 75° illumination geometries, it can be seen that although the proportion of diffuse irradiance increases with AOD, the SWA tends to decrease. The physical explanation for this decreased role of LSA with increasing AOD is that the direct radiation component is attenuated by strong atmospheric scattering at low solar angles.

Figures 4 and 5 show color contours of LUT values for broadband LSA versus AOD at 550 nm (horizontal axis) and SZA (vertical axis); with panels for a pristine atmosphere (AOD of 0.0), for a continental AOD of 1.0. AOD exceeding 1.0 (e.g., for large aerosol such as dust or cloud particles) is now not taken into account in the present LUT. But users can modify the LUT by adding cloud models into the RT code they employed.

Contrasts between Figs. 4(a) and 5(a) demonstrate that, for vegetated snow-free surfaces, response of GO kernel integral to SZA and AOD is much sharper than that for snow-covered surfaces. This is because vegetated surfaces have much more complex structures than snow cover, so that incident light has a larger

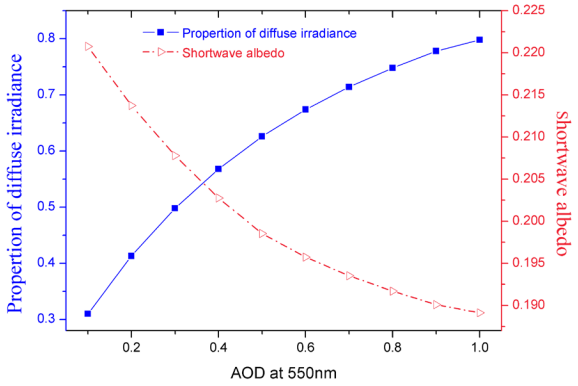


Fig. 3. Sensitivity of SWA to AOD at 550 nm.

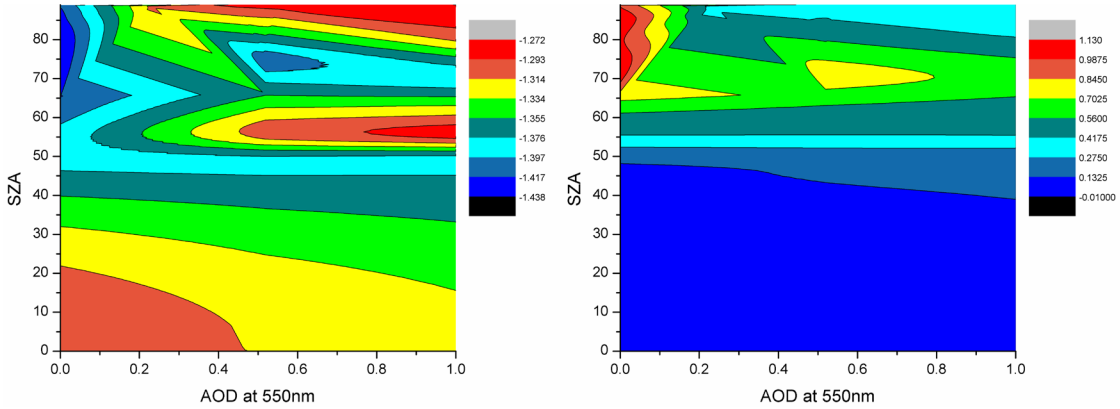


Fig. 4. Contour maps of (a) GO and (b) RTV BRDF kernel integrals versus SZA and AOD (550 nm) for snow-free cases.

possibility of escaping from snow grains without being absorbed, whereas the possibility of incident radiance escaping from vegetation canopy undergoes attenuation depending on the chlorophyll content of leaves.

A common feature can be found from Figs. 4(b) and 5(b), that is, sharp changes of $H_{\text{vol}}$ occur at a 50° SZA. For SZA at 55°, the value of $H_{\text{vol}}$ is the quadruple of that at 50° for snow-covered surfaces, whereas for snow-free surfaces, the value of $H_{\text{vol}}$ at 55° SZA is nearly 2.5 times the magnitude of that at 50°. With no emphasis on the accuracy of LSA estimate, it seems sound to treat distribution of diffuse skylight as isotropic. However, on the basis of our model results, the isotropic assumption may cause large biases at high latitudes where the sun is very low, especially in winter seasons. Hence, it is necessary for us to retrieve LSA with inclusion of diffuse sky radiation distribution at SZAs beyond 50°.

Based on the LUT (Fig. 5), the angular integrals of GO and RTV kernels modulated by the diffuse sky radiation distribution function $\Xi$ tend to decrease as the diffuse proportion increases with the increase in the SZA beyond 70°. This phenomenon is also observed in Ref. [22] and agrees well with Ref. [23]. Generally, the snow albedo tends to be more sensitive to SZA than to wind-driven structures. But when the SZA exceeds 70°, terrain-caused shapes and wind-driven zastrugi may have important effects on the decrease in snow albedo.

To evaluate the proposed anisotropic LSA model, we randomly selected 225 pixels from MODIS tile h26v04 to separately calculate SWA via Eq. (1) and MODIS isotropic SWA. MCD43A1 BRDF/albedo parameters were used as input for running our LSA model, whereas the MCD43A3 BSA and WSA data were combined linearly using the isotropic LSA model. It is important to keep in mind that we reject pixels which flagged as cloud, water, and those with low retrieving qualities based on the quality assessment data provided in MCD43A2. From the comparisons results (Fig. 6), one can see that neglecting the anisotropic diffuse skylight distribution at large SZAs can lead to –0.93% mean relative error. For some special cases, such as at high latitudes, the maximum relative bias can reach as much as 10% and even more for large AOD conditions.

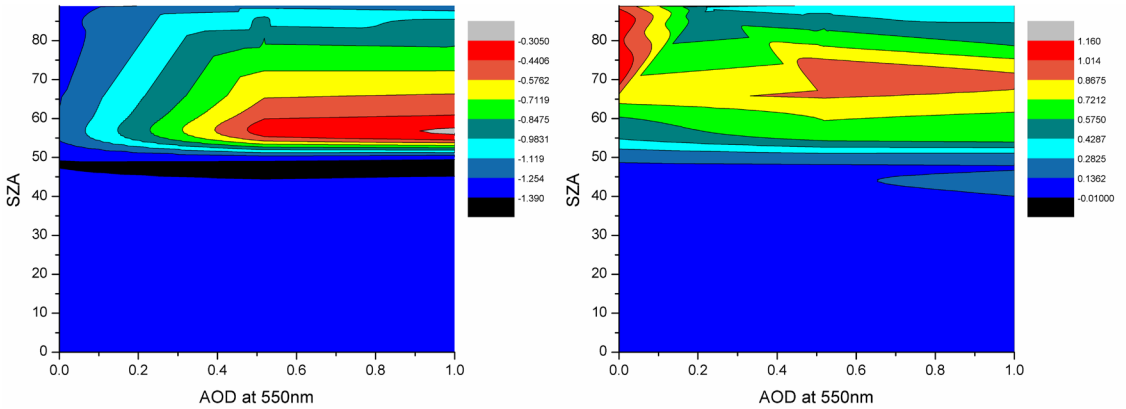


Fig. 5. Contour maps of (a) GO and (b) RTV BRDF kernel integrals versus SZA and AOD (550 nm) for snow-covered cases.

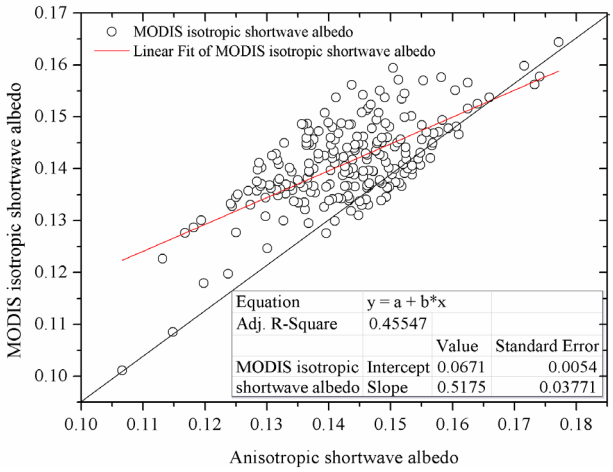


Fig. 6. Evaluation of the anisotropic shortwave LSA versus MODIS isotropic SWA.

In conclusion, we design a fast and accurate LSA parameterization scheme. We also develop the concept of angular distribution models of diffuse sky radiation to facilitate the parameterization and its applications. With the anisotropic LSA remote sensing model, the parameterization for LSA is implemented for vegetated snow-free and snow-covered surfaces, respectively. The directional–hemispherical and bi-hemispherical integrals for BRDF GO and RTV kernels are tabulated as functions of SZA and AOD, with inclusion of the anisotropic behaviors of diffuse sky radiation. With land surface BRDF model parameters retrieved from remotely sensed measurements, one can easily get spectral and broadband LSA. The parameterization scheme is designed in a flexible manner so that users can implant any satellite instrument's spectral response function into the model. It is a promising scheme for remote sensing and climate applications.

This work was supported by the National Natural Science Foundation of China (No. 41305019) and the Anhui Provincial Natural Science Foundation (No. 1308085QD70).

## References

1. R. J. Charlson, F. P. J. Valero, and J. H. Seinfeld, Science **308,** 806 (2005).
2. W. E. Heilman, D. Y. Hollinger, X. Li, X. Bian, and S. Zhong, Atmos. Sci. Lett. **11,** 319 (2010).
3. A. Cescatti, B. Marcolla, S. K. S. Vannan, J. Y. Pan, M. O. Román, X. Yang, P. Ciais, R. B. Cook, B. E. Law, G. Matteucci, M. Migliavacca, E. Moors, A. D. Richardson, G. Seufert, and C. B. Schaaf, Remote Sens. Environ. **121,** 323 (2012).
4. D. K. Hall and G. A. Riggs, Hydrol. Process. **21,** 1534 (2007).
5. K. Wang, S. Liang, C. L. Schaaf, and A. H. Strahler, J. Geophys. Res. **115,** D17107 (2010).
6. Y. Shuai, C. B. Schaaf, A. H. Strahler, J. Liu, and Z. Jiao, Geophys. Res. Lett. **35,** L05407 (2008).
7. S. Cui, S. Yang, Y. Qiao, Q. Zhao, J. Wang, and Z. Wang, Optik **123,** 250 (2012).
8. Z. Jin, Y. Qiao, Y. Wang, Y. Fang, and W. Yi, Opt. Express **19,** 26429 (2011).
9. Z. Jin, T. P. Charlock, W. L. Smith Jr., and K. Rutledge, Geophys. Res. Lett. **31,** L22301 (2004).
10. P. Lewis and M. J. Barnsley, in *Proceedings of the 6th International Symposium on Physical Measurements and Signatures in Remote Sensing* 707 (1994).
11. M. O. Román, C. B. Schaaf, P. Lewis, F. Gao, G. P. Anderson, J. L. Privette, A. H. Strahler, C. E. Woodcock, and M. Barnsley, Remote Sens. Environ. **114,** 738 (2010).
12. S. Cui, S. Yang, Y. Qiao, and Q. Zhao, J. Huazhong Univ. Sci. Technol. **39,** 41 (2011).
13. Z. Wang, S. Yang, Y. Qiao, S. Cui, and Q. Zhao, J. Quant. Spectrosc. Radiat. Transfer **112,** 2619 (2011).
14. Z. Wang, S. Yang, Y. Qiao, S. Cui, and Q. Zhao, Terr. Atmos. Ocean Sci. **23,** 59 (2012).
15. K. Stamnes, S. C. Tsay, W. Wiscombe, and I. Laszlo, "DISORT, a general-purpose Fortran program for discrete-ordinate-method radiative transfer in scattering and emitting layered media: documentation of methodology," Technical Report (Stevens Institute of Technology, 2000).
16. H. Iwabuchi, J. Atmos. Sci. **63,** 2324 (2006).
17. K. F. Evans, J. Atmos. Sci. **55,** 429 (1998).
18. A. I. Lyapustin, Appl. Opt. **44,** 7764 (2005).
19. C. Yang, L. Wei, J. Wu, and J. Leng, Chin. Opt. Lett. **5,** 125 (2007).
20. C. K. Gatebe, M. D. King, S. Platnick, G. T. Arnold, E. F. Vermote, and B. Schmid, J. Geophys. Res. **108,** 8489 (2003).
21. S. Liang, A. Strahler, and C. Walthall, J. Appl. Meteorol. **38,** 712 (1999).
22. S. Wuttke, G. Seckmeyer, and G. Konig-Lang, Ann. Geophys. **24,** 7 (2006).
23. A. S. Gardner and M. J. Sharp, J. Geophys. Res. **115,** F01009 (2010).